An Efficient Numerical Approach to Solve SEIR Epidemic of Measles of Fractional Order by Using Hermite Wavelets

NAGENDRA K. YADAV[1,2], RAJESH K. SINHA[1], RAKESH RANJAN[3,*], RAMSINGH YADAV[4]

[1]Department of Mathematics,
National Institute of Technology Patna,
Patna, Bihar-800005,
INDIA

[2]Department of Applied Science & Humanities,
Government Engineering College Gopalganj,
Science,Technology and Technical Education Department, Patna,
Gopalganj, Bihar-841501,
INDIA

[3]Department of Applied Science & Humanities,
Government Polytechnic Lakhisarai,
Science,Technology and Technical Education Department, Patna,
Lakhisarai, Bihar-811311,
INDIA

[4]Department of Applied Science & Humanities,
Motihari College of Engineering, Motihari,
Science,Technology and Technical Education Department, Patna,
Motihari, Bihar-845401,
INDIA

*Corresponding Author

Abstract: - Mathematical biology is a captivating field of applied mathematics that provides a precise understanding of biological occurrences and their connection to health related matters. Implementing novel mathematical methods and definitions in this field of study will significantly enhance public health by effectively managing certain diseases and utilizing the modern tools at our disposal is the most compelling justification for conducting novel research. In this study, Hermite wavelet and Adams-Bashforth-Moulton predictor-corrector (ABM) methods are employed to solve a nonlinear fractional SEIR measles epidemic model with unspecified parameters. The SEIR model is a set of differential equations used in medical science to investigate medical and epidemiology treatment for those affected. Operational matrices, when used in conjunction with the collocation method, convert fractional-order models into a system of algebraic equations. The Hermite wavelet method (HWM) is employed to graphically represent the chaotic attractors of the fractional SEIR model. The effectiveness of the Hermite wavelet method has been validated through an analysis of its convergence, error, and stability. Furthermore, we have conducted a comparison between solutions obtained using Hermite wavelets and the ABM method to evaluate the accuracy and suitability of the Hermite wavelet scheme.

Key-Words: - Caputo derivative, Hermite wavelets, ABM scheme, Operational matrix, Measles model

Received: September 13, 2024. Revised: January 2, 2025. Accepted: January 19, 2025. Published: March 28, 2025.

1 Introduction

Fractional calculus (FC) explores derivatives and integrals of arbitrary order, encompassing both real and complex domains. In recent decades, fractional differential equations (FDEs) have made substantial strides, driven largely by their broad applicability across various scientific and engineering disciplines. FDEs excel in accurately modeling real-world phenomena by mitigating errors caused by overlooked parameters. Various mathematical models incorporate fractional differential equations (FDEs), such as studies on hepatitis B virus [1], breast cancer [2], and Nipah Virus [3]. The study [4] examines the dengue model using FDEs, while [5], [6], and [7] address models related to rubella, food chains, and tuberculosis, respectively. Fractional calculus, despite its development more than 300 years ago, continues to be pertinent in contemporary times for resolving practical issues. The utilization of the Caputo derivative holds significant importance in the resolution of practical issues, as it facilitates the incorporation of conventional initial and boundary conditions inside problem formulations. The Caputo derivative differs from the typical derivative in that it is adjusted to account for initial conditions, which makes it particularly useful for modeling processes that display memory effects. The use of novel fractional operators in practical models has resulted in notable progress within this domain [1], [2], [3], [4], [8]. The classification of fractional operators is based on singular, non-singular, and nonlocal kernels [9], [10]. The Caputo, Caputo-Fabrizio, Atangana-Baleanu, Riemann-Liouville, Riesz, and Hadamard operators are among the often employed alternatives [9], [10], [11]. Numerous studies have frequently yielded suboptimal outcomes when employing integer-order operators, underscoring the need of novel differential operators in the representation of real-world scenarios. The utilization of the Caputo derivative enhances the accuracy of wavelet outputs.

In recent decades, numerous researchers have developed and applied mathematical models to study disease transmission within the field of mathematical epidemiology [12], [13]. The SEIR mathematical model extends the classical SIR model [14], which was presented by Kermack and McKendrick in 1927. In many infectious diseases, after the initial infection stage, there is a latent period before individuals become infectious, which is crucial to consider when analyzing the progression of the disease. Therefore, it make sense to include an initial compartment in the epidemiological model. This current SEIR model comprises four compartments representing different stages of the infectious disease: susceptible individuals $\mathcal{S}$, exposed individuals $\mathcal{E}$, infectious individuals $\mathcal{I}$, and recovered individuals $\mathcal{R}$. Various diseases exhibit periods where a portion of the infected population remains asymptomatic, and these conditions are typically modeled using SEIR frameworks [13], [15]. Mathematical epidemiological models are highly valuable for prevention, treatment, planning, and control programs [12], [16].

The SEIR model of fractional order in Caputo sense $({}_0^C\mathfrak{D}_t^\gamma)$ [11], [17], is given as

$$\begin{cases} {}_0^C\mathfrak{D}_t^\gamma\mathfrak{S}(t) = \mu - \sigma\mathfrak{S}\mathfrak{F} - \delta\mathfrak{S}, \\ {}_0^C\mathfrak{D}_t^\gamma\mathfrak{E}(t) = \sigma\mathfrak{S}\mathfrak{F} - (\varrho + \delta + \epsilon)\mathfrak{F}, \\ {}_0^C\mathfrak{D}_t^\gamma\mathfrak{F}(t) = \epsilon\mathfrak{E} - (\nu + \delta)\mathfrak{F}, \\ {}_0^C\mathfrak{D}_t^\gamma\mathfrak{R}(t) = \nu\mathfrak{F} + \varrho\mathfrak{E} - \delta\mathfrak{R}, \end{cases} \tag{1}$$

Here, birth rate (μ): This represents the rate at which new individuals are born into the population; Rate of recovery from infection (ν): This indicates how quickly infected individuals recover from the disease and become immune; rate of infected individual (σ): This denotes how easily the infection spreads from an infected individual to a susceptible (non-immune) individual;natural death rate (δ): This refers to the rate at which individuals die due to natural causes unrelated to the infection;rate of individuals becoming infected (ϵ): This could represent the rate at which susceptible individuals become infected when exposed to the disease;measles therapy rate (ϱ): In the context of measles, this might represent the rate at which infected individuals receive treatment or recover from symptoms.

Wavelets have become increasingly popular in numerous scientific fields such as computational sciences, physical, chemical, biological sciences, numerical analysis, signal analysis, image transformation, and data compression over the past few decades [15], [17], [18], [19], [20]. Wavelets have been extensively utilised for solving differential equations (DEs) and integro-differential equations since the 1980s. The primary characteristics of all wavelet-based approaches are to identify singularities, transitory phenomena, and irregular structures displayed by the investigated models. In 1912, SN Bernstein proposed the concepts of Bernstein polynomials. A Bernstein polynomial can be written as a linear combination of Bernstein basis polynomials. Although these Bernstein polynomials lack orthogonality, they possess other several beneficial characteristics [17]. These polynomials have been effectively applied for solving differential and integral equations in many scientific and engineering related domains. Additionally, A variety of analytic and numerical techniques have been used to effectively solve different types of FDEs, such as the fixed point method [21], [22], homotopy analysis method [16], Bernstein wavelets [17], Legendre wavelet [18], and Haar wavelet method [19]. In classical SEIR models, while widely used, but have limitations to capture the nuanced behaviour of epidemic systems with non-integral order dynamics, where memory and delayed effects play critical roles in transmission. This study aims to propose an effective numerical approach using Hermite wavelets for solving the nonlinear fractional order SEIR measles disease model. This approach offers enhanced accuracy and computational efficiency in simulating the transmission dynamics of measles, particularly related to real-world vaccination campaigns. Using block pulse functions, an operational matrix (HWOM) for R-L non-integer order integral operator in Hermite wavelets is derived, facilitating the transformation of this nonlinear SEIR measles system of fractional order into a system of algebraic equations. Furthermore, the ABM method is employed to compare solutions obtained using Hermite wavelets.

Here is the structure of the article: Section 2 covers essential definitions in FC. Section 3 focuses on generating Hermite wavelets across any interval and analyzing their convergence. Section 4 constructs the operational matrix for Hermite wavelets (HWOM) using block pulse functions. Section 5 applies Hermite wavelets and the ABM method to solve fractional order SEIR model. Section 6 provides a detailed analysis and simulation of numerical data, and Section 7 concludes with final remarks.

2 Definitions

Definition 1. Riemann-Liouville (RL) Integral operator for order κ is characterized as

$$\mathfrak{I}_t^{\kappa}\Theta(t) = \begin{cases} \frac{1}{\Gamma(\kappa)}\int_0^t \frac{\Theta(z)}{(t-z)^{1-\kappa}}dz = \frac{1}{\Gamma(\kappa)}t^{\kappa-1} * \Theta(t), & \kappa > 0, t > 0, \\ \Theta(t), & \kappa = 0, \end{cases} \tag{2}$$

here $t^{\kappa-1}*\Theta(t)$ is convolution multiplication of $t^{\kappa-1}$ and $\Theta(t)$.

Definition 2. Fractional derivatives of order κ in the Caputo's form is defined as follows

$${}_0^C\mathfrak{D}_t^{\kappa}\Theta(t) = \begin{cases} \frac{1}{\Gamma(n-\kappa)}\int\limits_0^t \frac{\Theta^{(n)}(z)}{(t-z)^{\kappa+1-n}}dz, & n-1 < \kappa \leq n, \ n \in \mathbb{N}. \end{cases} \tag{3}$$

3 Hermite wavelets and its characteristics

Let j, η be positive integers. The Hermite wavelets $\Lambda_{\aleph k}(t)$ for $\aleph = 1, 2, 3, ..., 2^{j-1}$ and $k = 0, 1, 2, ..., \eta - 1$ are described over $[0, t_l)$ as follows

$$\Lambda_{\aleph k}(t) = \begin{cases} \frac{2^{\frac{j+1}{2}}}{\sqrt{\pi}}\mathcal{W}_k(\frac{2^j}{t_l}t - 2\aleph + 1), & if, \frac{2\aleph-2}{2^j}t_l \leq t < \frac{2\aleph}{2^j}t_l, \\ 0, & otherwise, \end{cases} \tag{4}$$

where $\mathcal{W}_k(t)$ denotes Hermite polynomial [23], of degree k associated weight function $w(t) = \sqrt{1-t^2}$ over the real line $\mathbb{R}$, and it obeys the following recurresive relation.

$$\begin{aligned} \mathcal{W}_0(t) &= 1 \\ \mathcal{W}_1(t) &= 2t \\ \mathcal{W}_{k+2}(t) &= 2t\mathcal{W}_{k+1}(t) - 2(k+1)\mathcal{W}_k(t). \end{aligned}$$

Suppose $\Upsilon_{j,\eta}$, the space generated by Hermite wavelets for $\Lambda_{\aleph k}$, i.e. $\Upsilon_{j,\eta}$=span$\{\Lambda_{1,0}, \Lambda_{2,0}, ..., \Lambda_{2^{j-1},0}, \Lambda_{1,1}, ..., \Lambda_{2^{j-1},1}, \Lambda_{2,2}, ..., \Lambda_{2^{j-1},2}, ..., \Lambda_{2^{j-1},\eta}\}$ $\subseteq L^2(0,1)$. Taking Ω an arbitrary element belonging to $L^2(0,1)$. Then, Ω possesses a unique optimal approximation from $\Upsilon_{j,\eta}$ characterized by $\Omega_0 \in \Upsilon_{j,\eta}$,

$$\forall \chi \in \Upsilon_{j,\eta}, \qquad \|\Omega - \Omega_0\| \leq \|\Omega - \chi\|.$$

Since $\Omega_0 \in \Upsilon_{j,\eta}$ possesses a unique optimal approximation then there exist unique coefficients

$$Q_{1,0}, Q_{2,0}, \ldots, Q_{2^{j-1},0}, Q_{1,1}, \ldots, Q_{2^{j-1},1}, Q_{2,2}, \ldots, Q_{2^{j-1},2}, \ldots, Q_{2^{j-1},\eta}$$

such that

$$\Omega(t) \simeq \Omega_0(t) = \sum_{\aleph=1}^{2^{j-1}}\sum_{k=0}^{\eta-1} Q_{\aleph k}\Lambda_{\aleph k}(t) = Q^T F, \tag{5}$$

where Q and F column vectors described as

$$Q^T = \big[Q_{1,0}, Q_{2,0}, \ldots, Q_{2^{j-1},0}, Q_{1,1}, \ldots, Q_{2^{j-1},1}, Q_{1,2}, \ldots, Q_{2^{j-1},2}, \ldots, Q_{2^{j-1},\eta}\big]$$

and

$$F^T = [\Lambda_{1,0}, \Lambda_{2,0}, \ldots, \Lambda_{2^{j-1},0}, \Lambda_{1,1}, \ldots, \Lambda_{2^{j-1},1}, \Lambda_{2,2}, \ldots, \Lambda_{2^{j-1},2}, \ldots, \Lambda_{2^{j-1},\eta}].$$

Selecting $j = 2$, $\eta = 4$ and collocation points such as $t_n = \frac{2n-1}{2\hat{k}}$, $n = 1, 2, ..., \hat{k} = 2^{j-1}\eta$, we get Hermite wavelet matrix (HWM) as

$$\Psi_{8\times8} = \begin{pmatrix} 1.5958 & 1.5958 & 1.5958 & 1.5958 & 0 & 0 & 0 & 0 \\ 0 & 0 & 0 & 0 & 1.5958 & 1.5958 & 1.5958 & 1.5958 \\ -2.3937 & -0.7979 & 0.7979 & 2.3937 & 0 & 0 & 0 & 0 \\ 0 & 0 & 0 & 0 & -2.3937 & -0.7979 & 0.7979 & 2.3937 \\ 0.3989 & -2.7926 & -2.7926 & 0.3989 & 0 & 0 & 0 & 0 \\ 0 & 0 & 0 & 0 & 0.3989 & -2.7926 & -2.7926 & 0.3989 \\ 9.5995 & 2.6679 & -4.0642 & -9.4001 & 0 & 0 & 0 & 0 \\ 0 & 0 & 0 & 0 & 9.7990 & 1.2716 & -5.4605 & -9.2006 \end{pmatrix}$$

Theorem 1. *Assume $\Omega(t) \in L^2[0, t_l]$ be a function and suppose $\Omega(t)$ approximated by $\Omega_0(t) \in \Upsilon_{j,\eta}$ then*

$$\|\epsilon_\Omega\| = \|\Omega(t) - \Omega_0(t)\| < \mathcal{B}t_l^{\frac{2\eta+1}{2}}(\eta!\sqrt{2\eta+1})^{-1}.$$

Proof. Let $\Omega^{(n)}(t)$ are the continuous functions, where $n = 0, 1, 2, ...\eta$. Then there exists $\mathcal{B} \in \mathbb{N}$ such that

$$\Omega^{(n)}(t) < \mathcal{B}, \quad \forall \quad t \in [0, t_l].$$

Now by applying Taylor$'$s formula

$$\Omega(t) = \sum_{n=0}^{\eta-1} \frac{\Omega^n(0)t^n}{n!} + \frac{\Omega^{(\eta)}(\xi)}{\eta!} t^\eta, \quad where \ \ \xi \in [0, t_l].$$

Here, $\{\Lambda_{\aleph k}(t)\}$ represents a family of piecewise functions. As $\Upsilon_{j,\eta} = span\{\Lambda_{\aleph k}(t)\}$, therefore

$$\sum_{0}^{\eta-1} \frac{\Omega^{(n)}(0)t^n}{n!} \in \Upsilon_{j,\eta},$$

Since $\Omega_0(t)$ is the optimal approximation of $\Omega(t)$ among $\Upsilon_{j,\eta}$, then

$$\begin{aligned}
\|\epsilon_\Omega\| &= \|\Omega(t) - \Omega_0(t)\| \\
&\leq \Big\|\Omega(t) - \sum_{0}^{\eta-1} \frac{\Omega^{(n)}(0)t^n}{n!}\Big\| \\
&= \Big\|\frac{\Omega^{(\eta)}(\xi)t^\eta}{\eta!}\Big\| = \Big(\int_0^{t_l} \Big(\frac{\Omega^{(\eta)}(\xi)t^\eta}{\eta!}\Big)^2\Big)^{\frac{1}{2}} \\
&< \Big(\frac{\mathcal{B}^2 t_l^{2\eta+1}}{(\eta!)^2(2\eta+1)}\Big)^{\frac{1}{2}} = \mathcal{B} t_l^{\frac{2\eta+1}{2}} (\eta!\sqrt{2\eta+1})^{-1}
\end{aligned}$$

here $t_l \in \mathbb{N}$ is a fixed natural number and as η sufficiently big number then $\|\epsilon_\Omega\| \to 0$. And thus Hermite wavelets approximation converges. □

Theorem 2. *Let* $\Theta(t) \in C^{\mathfrak{J}+1}[0, 1]$ *and* $\mathcal{P}_{\mathfrak{J}}^{2^{\mathfrak{K}}-1}\Theta(t)$, *where* $\mathcal{P}_{\mathfrak{J}}^{2^{\mathfrak{K}}-1}\Theta(t) = \sum_{\aleph=0}^{2^{\mathfrak{K}}-1} \sum_{k=0}^{\mathfrak{J}} \xi_{\aleph,k}\varphi_{\aleph,k}(t)$ *is the solution approximated by utilising Hermite wavelets then the error bound given by*

$$\|\mathcal{E}(t)\| \leq \Big\|\frac{\beta}{(\mathfrak{J}+1)!2^{(\mathfrak{J}+1)(\mathfrak{K}+1)-1}}\Big\|,$$

here $\mathcal{E}(t) = |\Theta(t) - \sum_{\aleph=0}^{2^{\mathfrak{K}}-1} \sum_{k=0}^{\mathfrak{J}} \xi_{\aleph,k}\varphi_{\aleph,k}(t)|$ *and* $\beta = Max_{t\in[0,1)}|\Theta^{\mathfrak{J}+1}(t)|$.

Proof: Considering the notion of norm in an inner product space, we obtain

$$\|\mathcal{E}(t)\|^2 = \int_0^1 \Big|\Theta(t) - \mathcal{P}_{\mathfrak{J}}^{2^{\mathfrak{K}}-1}\Theta(t)\Big|^2 dt.$$

Now, partitioning into $2^{\mathfrak{K}}$ sub-intervals $I_\aleph = \left[\frac{\aleph}{2^{\mathfrak{K}}}, \frac{\aleph+1}{2^{\mathfrak{K}}}\right]$, $\aleph = 0, 1, 2, ..., 2^{\mathfrak{K}} - 1$.

$$\|\mathcal{E}(t)\|^2 = \sum_{\aleph=0}^{2^{\mathfrak{K}}-1} \int_{\frac{\aleph}{2^{\mathfrak{K}}}}^{\frac{\aleph+1}{2^{\mathfrak{K}}}} \Big|\Theta(t) - \mathcal{P}_{\mathfrak{J}}\mathfrak{J}^{2^{\mathfrak{K}}-1}\Theta(t)\Big|^2 dt,$$

$$\|\mathcal{E}(t)\|^2 = \sum_{\aleph=0}^{2^{\mathfrak{K}}-1} \int_{\frac{\aleph}{2^{\mathfrak{K}}}}^{\frac{\aleph+1}{2^{\mathfrak{K}}}} \Big|\Theta(t) - \mathcal{P}_{\mathfrak{J}+1}(t)\Big|^2 dt,$$

The expression $\mathcal{P}_{\mathfrak{J}+1}(t)$ is the interpolated polynomial of degree $\mathfrak{J} + 1$ that provides an approximation of $\Theta(t)$ within the interval $I_\aleph$.Utilising the polynomial on $I_\aleph$ maximum error estimate, we arrive at

$$\|\mathcal{E}(t)\|^2 \leq \sum_{\aleph=0}^{2^{\mathfrak{K}}-1} \int_{\frac{\aleph}{2^{\mathfrak{K}}}}^{\frac{\aleph+1}{2^{\mathfrak{K}}}} \Big|\frac{Max_{t\in L^2[0,1)}|\Theta^{\mathfrak{J}+1}(t)|}{(\mathfrak{J}+1)!2^{(\mathfrak{J}+1)(\mathfrak{K}+1)-1}}\Big|^2 dt,$$

$$\|\mathcal{E}(t)\|^2 \leq \sum_{\aleph=0}^{2^{\mathfrak{K}}-1} \int_{\frac{\aleph}{2^{\mathfrak{K}}}}^{\frac{\aleph+1}{2^{\mathfrak{K}}}} \Big|\frac{\beta}{(\mathfrak{J}+1)!2^{(\mathfrak{J}+1)(\mathfrak{K}+1)-1}}\Big|^2 dt,$$

$$\|\mathcal{E}(t)\|^2 \leq \int_0^1 \Big|\frac{\beta}{(\mathfrak{J}+1)!2^{(\mathfrak{J}+1)(\mathfrak{K}+1)-1}}\Big|^2 dt.$$

And thus we have,

$$\|\mathcal{E}(t)\| \leq \Big\|\frac{\beta}{(\mathfrak{J}+1)!2^{(\mathfrak{J}+1)(\mathfrak{K}+1)-1}}\Big\|.$$

4 Operational matrix associated with Hermite wavelets

In this part, we develop the operational matrices of Hermite wavelets for both integer and fractional order integrations. These matrices play a pivotal role in our proposed solution method for addressing the problem at hand.

By the utilization of the Block Pulse function -
Over the interval $[0, t_l)$, the block pulse functions (BPFs) are defined as

$$\beta_j(t) = \begin{cases} 1, & if, \ \frac{jt_l}{\hat{k}} \leq t < \frac{(j+1)t_l}{\hat{k}}, \\ 0, & otherwise, \end{cases} \quad (6)$$

where $j = 0, 1, 2, ..., \hat{k}$ and $\mathcal{B}_{\hat{k}} = [\beta_1, \beta_2, \beta_3, ..., \beta_{\hat{k}}]$.The beneficial characteristics of BPFs are enumerated in [24]. In this work, BPFs will be employed for constructing the operational matrix of non-integer order integration for Hermite wavelets.

$$(I_t^\alpha \mathcal{B}_{\hat{k}})(t) \cong \Xi^\alpha \mathcal{B}_{\hat{k}},$$

$$\Xi^{\alpha}_{\hat{k}\times\hat{k}} = \frac{t_l^{\alpha}}{\hat{k}^{\alpha}\Gamma(\alpha+2)} \begin{pmatrix} 1 & \rho_1 & \rho_2 & \rho_3 & \cdots & \rho_{\hat{k}-1} \\ 0 & 1 & \rho_1 & \rho_2 & \cdots & \rho_{\hat{k}-2} \\ 0 & 0 & 1 & \rho_1 & \cdots & \rho_{\hat{k}-3} \\ \vdots & \vdots & \ddots & \ddots & & \vdots \\ 0 & 0 & \ldots & 0 & 1 & \rho_1 \\ 0 & 0 & \ldots & 0 & 0 & 1 \end{pmatrix}. \tag{7}$$

and $\rho_l = (p+1)^{\alpha+1} - 2p^{\alpha+1} + (p-1)^{\alpha+1}$, for $p = 1, 2, 3, ..., \hat{k}-1$.

Next, we derive the operating matrix for arbitrary order integration of Hermite wavelets., P^{α}. Let

$$(I_t^{\alpha}\Lambda)(t) \cong P^{\alpha}\Lambda(t).$$

Then,

$$\begin{aligned}(I_t^{\alpha}\Lambda)(t) \cong& (I_t^{\alpha}\Lambda\mathcal{B}_{\hat{k}})(t) = \Lambda(I_t^{\alpha}\mathcal{B}_{\hat{k}})(t) \\ \approx& \Lambda\Xi^{\alpha}\mathcal{B}_{\hat{k}}.\end{aligned}$$

Hence,

$$\begin{aligned}P^{\alpha}\Lambda(t) \cong& \Lambda(t)\Xi^{\alpha}\mathcal{B}_{\hat{k}} \\ P^{\alpha} =& \Psi_{\hat{k}\times\hat{k}}\Xi^{\alpha}\Psi^{-1}_{\hat{k}\times\hat{k}}.\end{aligned}$$

By using above mentioned fact the HWOM P^{α} for $\alpha = 0.95$, $\eta = 4$, $j = 2$ and $t_l = 1$ will be given as

$$P^{\alpha}_{8\times8} = \begin{pmatrix} 0.2694 & 0.5060 & 0.1376 & -0.0141 & -0.0028 & 0.0038 & 0.0017 & -0.0016 \\ 0 & 0.2694 & 0 & 0.1376 & 0 & -0.0045 & 0 & 0.0017 \\ -0.1115 & 0.0106 & -0.0140 & -0.0101 & 0.0723 & 0.0037 & -0.0061 & -0.0017 \\ 0 & -0.1115 & 0 & -0.0140 & 0 & 0.0784 & 0 & -0.0061 \\ -0.1999 & -0.3777 & 0.5953 & 0.0064 & -0.0868 & -0.0012 & 0.1878 & 0.0004 \\ 0 & -0.1999 & 0 & 0.5953 & 0 & -0.2746 & 0 & 0.1878 \\ 0.3407 & -0.2311 & 0.3685 & 0.0432 & -0.3390 & -0.0153 & 0.1218 & 0.0069 \\ 0 & 0.1409 & 0 & 0.9638 & 0 & -0.7355 & 0 & 0.3096 \end{pmatrix}.$$

The square matrix $P^{\alpha}_{8\times8}$ shown above represents an operational matrix derived from the Hermite wavelet with a parameter value of $\alpha = 0.95$.Additionally, it is possible to obtain the HWOM for any value of α within the range of $0 < \alpha \leq 1$. If we increase the values of η and j, the matrix order increases. A higher-order matrix incorporates additional basis functions, capturing more intricate dynamics of the model and potentially improving the approximation's fidelity.

5 Methods proposed for the fractional SEIR epidemic model

5.1 Utilizing Hermite wavelets to numerically solve SEIR model

Examine the SEIR epidemic model given in equation (1). We incorporate higher-order fractional derivatives using Bernstein wavelets, as outlined below:

$$\begin{cases} {}_0^C D_\tau^{\gamma}\mathfrak{S}(t) = Q_1^T F, \\ {}_0^C D_\tau^{\gamma}\mathfrak{E}(t) = Q_2^T F, \\ {}_0^C D_\tau^{\gamma}\mathfrak{F}(t) = Q_3^T F, \\ {}_0^C D_\tau^{\gamma}\mathfrak{R}(t) = Q_4^T F. \end{cases} \tag{8}$$

Here, $Q_i^T = [Q_{00}^i, Q_{01}^i, ..., Q_{0,\eta}^i, Q_{1,0}^i, ..., Q_{1\eta}^i, Q_{(2^j-1)0}^i, ..., Q_{(2^j-1)\eta}^i]$ are unknowns for $i = 1, 2, 3, 4$.

Next, we apply the fractional integral operator to equation (8) in the Riemann-Liouville sense, resulting in:

$$\begin{cases} (I_t^{\gamma}\,{}_0^C D_t^{\gamma})(\mathfrak{S}(t)) = Q_1^T G(t,\gamma), \\ (I_t^{\gamma}\,{}_0^C D_t^{\gamma})(\mathfrak{E}(t)) = Q_2^T G(t,\gamma), \\ (I_t^{\gamma}\,{}_0^C D_t^{\gamma})(\mathfrak{F}(t)) = Q_3^T G(t,\gamma), \\ (I_t^{\gamma}\,{}_0^C D_t^{\gamma})(\mathfrak{R}(t)) = Q_4^T G(t,\gamma). \end{cases} \tag{9}$$

Also,

$$\begin{cases} (I_t^{\gamma}\,{}_0^C D_t^{\gamma})(\mathfrak{S}(t)) = \mathfrak{S}(t) - \mathfrak{S}(0) = Q_1^T Q(t,\gamma), \\ (I_t^{\gamma}\,{}_0^C D_t^{\gamma})(\mathfrak{E}(t)) = \mathfrak{E}(t) - \mathfrak{E}(0) = Q_2^T Q(t,\gamma), \\ (I_t^{\gamma}\,{}_0^C D_t^{\gamma})(\mathfrak{F}(t)) = \mathfrak{F}(t) - \mathfrak{F}(0) = Q_3^T Q(t,\gamma), \\ (I_t^{\gamma}\,{}_0^C D_t^{\gamma})(\mathfrak{R}(t)) = \mathfrak{R}(t) - \mathfrak{R}(0) = Q_4^T Q(t,\gamma). \end{cases} \tag{10}$$

Then

$$\begin{cases} \mathfrak{S}(t) = \mathfrak{S}(0) + Q_1^T G(t,\gamma), \\ \mathfrak{E}(t) = \mathfrak{E}(0) + Q_2^T G(t,\gamma), \\ \mathfrak{F}(t) = \mathfrak{F}(0) + Q_3^T G(t,\gamma), \\ \mathfrak{R}(t) = \mathfrak{R}(0) + Q_4^T G(t,\gamma). \end{cases} \tag{11}$$

here only Q_i^T are the unknowns. By substituting the values of $\mathfrak{S}$,$\mathfrak{E}$, $\mathfrak{F}$ and $\mathfrak{R}$ into main equations mentioned in (1) and applying the collocation points $\frac{2n-1}{2\hat{k}}$, where $n = 1, 2, ..., 2^j(\eta+1)$, we get a collection of non-linear algebraic equations involving $3\hat{k}$ unknowns. Using Matlab to apply the Newton iteration method to these equations allows us to compute the unknown Bernstein coefficients.And By substituting unknowns coefficients in equation (11), we get the required solutions.

5.2 The Adams-Bashforth-Moulton method to numerically solve the SEIR epidemic model

By applying the ABM method to equation (1), we obtain the predictor values and their respective corrector values, as detailed below, in order to reformulate it into a distinct form;

Let $h = \frac{1-0}{\hat{k}}, t_n = nh, n = 0, 1, 2, ..., \hat{k} - 1,$

$$\begin{aligned}
\mathfrak{S}_{n+1} =& \mathfrak{S}(0) + \frac{h^\gamma}{\Gamma(\gamma+2)}(\mu - \sigma\mathfrak{S}^\beta_{n+1}\mathfrak{F}^\beta_{n+1} - \delta\mathfrak{S}^\beta_{n+1}) \\
&+ \frac{h^\gamma}{\Gamma(\gamma+2)}\sum_{i=0}^{n} p_{i,n+1}(\mu - \sigma\mathfrak{S}_i\mathfrak{F}_i - \delta\mathfrak{S}_i), \\
\mathfrak{E}_{n+1} =& \mathfrak{E}(0) + \frac{h^\gamma}{\Gamma(\gamma+2)} * \\
&(\sigma\mathfrak{S}^\beta_{n+1}\mathfrak{F}^\beta_{n+1} - (\varrho+\delta+\epsilon)\mathfrak{F}^\beta_{n+1}) \\
&+ \frac{h^\gamma}{\Gamma(\gamma+2)} * \\
&\sum_{i=0}^{n} p_{i,n+1}(\sigma\mathfrak{S}_i\mathfrak{F}_i - (\varrho+\delta+\epsilon)\mathfrak{F}_i), \\
\mathfrak{F}_{n+1} =& \mathfrak{F}(0) + \frac{h^\gamma}{\Gamma(\gamma+2)}(\epsilon\mathfrak{E}^\beta_{n+1} - (\nu+\delta)\mathfrak{F}^\beta_{n+1}) \\
&+ \frac{h^\gamma}{\Gamma(\gamma+2)}\sum_{i=0}^{n} p_{i,n+1}(\epsilon\mathfrak{E}_i - (\nu+\delta)\mathfrak{F}_i), \\
\mathfrak{R}_{n+1} =& \mathfrak{R}(0) + \frac{h^\gamma}{\Gamma(\gamma+2)}(\nu\mathfrak{F}^\beta_{n+1} - \varrho\mathfrak{E}^\beta_{n+1} - \delta\mathfrak{R}^\beta_{n+1}) \\
&+ \frac{h^\gamma}{\Gamma(\gamma+2)}\sum_{i=0}^{n} p_{i,n+1}(\nu\mathfrak{F}_i + \varrho\mathfrak{E}_i - \delta\mathfrak{R}_i), \\
\mathfrak{S}^\beta_{n+1} =& \mathfrak{S}(0) + \frac{1}{\Gamma(\gamma)}\sum_{i=0}^{n} q_{i,n+1}(\mu - \sigma\mathfrak{S}_i\mathfrak{F}_i - \delta\mathfrak{S}_i), \\
\mathfrak{E}^\beta_{n+1} =& \mathfrak{I}(0) + \frac{1}{\Gamma(\gamma)}\sum_{i=0}^{n} q_{i,n+1}(\sigma\mathfrak{S}_i\mathfrak{F}_i - (\varrho+\delta+\epsilon)\mathfrak{F}_i), \\
\mathfrak{F}^\beta_{n+1} =& \mathfrak{H}(0) + \frac{1}{\Gamma(\gamma)}\sum_{i=0}^{n} q_{i,n+1}(\epsilon\mathfrak{E}_i - (\nu+\delta)\mathfrak{F}_i), \\
\mathfrak{R}^\beta_{n+1} =& \mathfrak{V}(0) + \frac{1}{\Gamma(\gamma)}\sum_{i=0}^{n} q_{i,n+1}(\nu\mathfrak{F}_i + \varrho\mathfrak{E}_i - \delta\mathfrak{R}_i),
\end{aligned}$$

here,

$$p_{i,n+1} = \begin{cases} n^{\gamma+1} - (n-\gamma)(n+1)^\gamma, \quad if \;\; i = 0, \\ (n-i+2)^{\gamma+1} + (n-i)^{\gamma+1} - 2(n-i+1)^{\gamma+1}, \\ if \;\; 0 \le i \le n, \\ 1, \quad if \;\; i = 1, \end{cases}$$

$$q_{i,n+1} = \frac{h^\gamma}{\gamma}((n+1-i)^\gamma - (n-i)^\gamma), \quad 0 \le i \le n.$$

6 Stability Analysis-

6.1 The nonlinear model SEIR with fractional-order Caputo derivative.

Developing precise answers is a difficult task due to the non-linear nature of the SEIR system. Consequently, we have devised an iterative methodology to ascertain unique answer. To address this issue, a fractional order SEIR dynamical system has been designed.

$$\begin{aligned}
&{}^C_0\mathfrak{D}^\gamma_t\mathfrak{S}(t) = \mu - \sigma\mathfrak{S}(t)\mathfrak{F}(t) - \delta\mathfrak{S}(t), \mathfrak{S}(0) > 0 \\
&{}^C_0\mathfrak{D}^\gamma_t\mathfrak{E}(t) = \sigma\mathfrak{S}(t)\mathfrak{F}(t) - (\varrho+\delta+\epsilon)\mathfrak{F}(t), \mathfrak{E}(0) > 0 \\
&{}^C_0\mathfrak{D}^\gamma_t\mathfrak{F}(t) = \epsilon\mathfrak{E}(t) - (\nu+\delta)\mathfrak{F}(t), \mathfrak{F}(0) > 0 \qquad (12) \\
&{}^C_0\mathfrak{D}^\gamma_t\mathfrak{R}(t) = \nu\mathfrak{F}(t) + \varrho\mathfrak{E}(t) - \delta\mathfrak{R}(t), \mathfrak{R}(0) > 0.
\end{aligned}$$

with intial conditions

$$\mathfrak{S}_0 = 600,\ \mathfrak{E}_0 = 250,\ \mathfrak{F}_0 = 100,\ \mathfrak{R}_0 = 50. \quad (13)$$

By applying the Laplace Transform and then the Inverse Laplace Transform to both sides of the equation, we obtain

$$\begin{aligned}
\mathfrak{S}(t) =& \mathfrak{S}(0) + L^{-1}\{\frac{1}{s^\gamma}L\{\mu - \sigma\mathfrak{S}(t)\mathfrak{F}(t) - \delta\mathfrak{S}(t)\}\}, \\
\mathfrak{E}(t) =& \mathfrak{E}(0) + L^{-1}\{\frac{1}{s^\gamma}L\{\sigma\mathfrak{S}(t)\mathfrak{F}(t) - (\varrho+\delta+\epsilon)\mathfrak{F}(t)\}\}, \\
\mathfrak{F}(t) =& \mathfrak{F}(0) + L^{-1}\{\frac{1}{s^\gamma}L\{\epsilon\mathfrak{E}(t) - (\nu+\delta)\mathfrak{F}(t)\}\}, \\
\mathfrak{R}(t) =& \mathfrak{R}(0) + L^{-1}\{\frac{1}{s^\gamma}L\{\nu\mathfrak{F}(t) + \varrho\mathfrak{E}(t) - \delta\mathfrak{R}(t)\}\}.
\end{aligned} \quad (14)$$

Furthermore, presented below is the iterative formula:

$$\begin{aligned}
\mathfrak{S}_{\mathfrak{N}}(t) =& \mathfrak{S}(0) + L^{-1}\{\frac{1}{s^\gamma}L\{\mu - \sigma\mathfrak{S}_{\mathfrak{N}-1}(t)\mathfrak{F}_{\mathfrak{N}-1}(t) \\
&- \delta\mathfrak{S}_{\mathfrak{N}-1}(t)\}\}, \\
\mathfrak{E}_{\mathfrak{N}}(t) =& \mathfrak{E}(0) + L^{-1}\{\frac{1}{s^\gamma}L\{\sigma\mathfrak{S}_{\mathfrak{N}-1}(t)\mathfrak{F}_{\mathfrak{N}-1}(t) \\
&- (\varrho+\delta+\epsilon)\mathfrak{F}_{\mathfrak{N}-1}(t)\}\}, \\
\mathfrak{F}_{\mathfrak{N}}(\top) =& \mathfrak{F}(0) + L^{-1}\{\frac{1}{s^\gamma}L\{\epsilon\mathfrak{E}_{\mathfrak{N}-1}(t) - (\nu+\delta)\mathfrak{F}_{\mathfrak{N}-1}(t)\}\}, \\
\mathfrak{R}_{\mathfrak{N}}(\top) =& \mathfrak{R}(0) + L^{-1}\{\frac{1}{s^\gamma}L\{\nu\mathfrak{F}_{\mathfrak{N}-1}(t) + \varrho\mathfrak{E}_{\mathfrak{N}-1}(t) \\
&- \delta\mathfrak{R}_{\mathfrak{N}-1}(t)\}\}. \qquad (15)
\end{aligned}$$

As $\mathfrak{N} \longrightarrow \infty$,we get an approximation of the solution.

$$\begin{aligned}
\mathfrak{S}(t) &= lim_{\mathfrak{N}\longrightarrow\infty}\mathfrak{S}_{\mathfrak{N}}(t), \\
\mathfrak{E}(t) &= lim_{\mathfrak{N}\longrightarrow\infty}\mathfrak{E}_{\mathfrak{N}}(t), \\
\mathfrak{F}(t) &= lim_{\mathfrak{N}\longrightarrow\infty}\mathfrak{F}_{\mathfrak{N}}(t), \\
\mathfrak{R}(t) &= lim_{\mathfrak{N}\longrightarrow\infty}\mathfrak{R}_{\mathfrak{N}}(t). \qquad (16)
\end{aligned}$$

6.2 Stability analysis of the iterative approach

Theorem 3. *We demonstrate that the recursive strategy described by equation* (15) *is stable.*

Proof. Now there are four positive constants $\mu_1, \mu_2, \mu_3, \mu_4$ such that,

$$\begin{aligned} &\|\mathfrak{S}(t)\| < \mu_1,\\ &\|\mathfrak{E}(t)\| < \mu_2,\\ &\|\mathfrak{F}(t)\| < \mu_3, \qquad 0 \le t < T < \infty,\\ &\|\mathfrak{R}(t)\| < \mu_4. \end{aligned} \tag{17}$$

Furthermore, we consider a division of $C_2((a,b),(0,T))$ characterized by,

$$\Gamma = \left\{ \xi : (a,b)(0,T) \longrightarrow \frac{1}{\Gamma\gamma}\int_0^t (t-\xi)^{\gamma-1} * X(\xi)\, Y(\xi)\, d\xi \right\}. \tag{18}$$

Here, we define the following operator Φ characterized as.

$$\Phi(\mathfrak{S},\mathfrak{E},\mathfrak{F},\mathfrak{R}) = \begin{cases} \mu - \sigma\mathfrak{S}(t)\mathfrak{F}(t) - \delta\mathfrak{S}(t),\\ \sigma\mathfrak{S}(t)\mathfrak{F}(t) - (\varrho+\delta+\epsilon)\mathfrak{F}(t),\\ \epsilon\mathfrak{E}(t) - (\nu+\delta)\mathfrak{F}(t),\\ \nu\mathfrak{F}(t) + \varrho\mathfrak{E}(t) - \delta\mathfrak{R}(t). \end{cases} \tag{19}$$

Then after

$$= \begin{cases} < \Phi(\mathfrak{S},\mathfrak{E},\mathfrak{F},\mathfrak{R}) - \Phi(\mathfrak{S}_1,\mathfrak{E}_1,\mathfrak{F}_1,\mathfrak{R}_1),\\ (\mathfrak{S}-\mathfrak{S}_1, \mathfrak{E}-\mathfrak{E}_1, \mathfrak{F}-\mathfrak{F}_1, \mathfrak{R}-\mathfrak{R}_1) >\\ < \mu - \sigma(\mathfrak{S}(t)-\mathfrak{S}_1(t))(\mathfrak{F}(t)-\mathfrak{F}_1(t)) - \delta(\mathfrak{S}(t)-\mathfrak{S}_1(t)) >,\\ < \sigma(\mathfrak{S}(t)-\mathfrak{S}_1(t))(\mathfrak{F}(t)-\mathfrak{F}_1(t))\\ -(\varrho+\delta+\epsilon)(\mathfrak{F}(t)-\mathfrak{F}_1(t)) >,\\ < \epsilon(\mathfrak{E}(t)-\mathfrak{E}_1(t)) - (\nu+\delta)(\mathfrak{F}(t)-\mathfrak{F}_1(t)) >,\\ < \nu(\mathfrak{F}(t)-\mathfrak{F}_1(t)) + \varrho(\mathfrak{E}(t)-\mathfrak{E}_1(t)) - \delta(\mathfrak{R}(t)-\mathfrak{R}_1(t)) > . \end{cases} \tag{20}$$

Here,

$$\mathfrak{S}(t) \neq \mathfrak{S}_1(t), \;\; \mathfrak{E}(t) \neq \mathfrak{E}_1(t),, \;\; \mathfrak{F}(t) \neq \mathfrak{F}_1(t) \;\; \mathfrak{R}(t) \neq \mathfrak{R}_1(t). \tag{21}$$

$$< \begin{cases} \{\frac{\mu}{\|\mathfrak{S}(t)-\mathfrak{S}_1(t)\|^2} - \frac{\sigma\|\mathfrak{F}(t)-\mathfrak{F}_1(t)\|}{\|\mathfrak{S}(t)-\mathfrak{S}_1(t)\|} - \frac{\delta}{\|\mathfrak{S}(t)-\mathfrak{S}_1(t)\|}\}\\ \|\mathfrak{S}(t)-\mathfrak{S}_1(t)\|^2,\\ \{\frac{\sigma\|\mathfrak{S}(t)-\mathfrak{S}_1(t)\|\|\mathfrak{F}(t)-\mathfrak{F}_1(t)\|}{\|\mathfrak{E}(t)-\mathfrak{E}_1(t)\|^2}\\ -\frac{(\varrho+\delta+\epsilon)\|\mathfrak{F}(t)-\mathfrak{F}_1(t)\|}{\|\mathfrak{E}(t)-\mathfrak{E}_1(t)\|^2}\}\|\mathfrak{E}(t)-\mathfrak{E}_1(t)\|^2,\\ \{\frac{\epsilon\|\mathfrak{E}(t)-\mathfrak{E}_1(t)\|}{\|\mathfrak{F}(t)-\mathfrak{F}_1(t)\|^2} - \frac{(\nu+\delta)}{\|\mathfrak{F}(t)-\mathfrak{F}_1(t)\|}\}\|\mathfrak{F}(t)-\mathfrak{F}_1(t)\|^2,\\ \{\frac{\nu\|\mathfrak{F}(t)-\mathfrak{F}_1(t)\|}{\|\mathfrak{R}(t)-\mathfrak{R}_1(t)\|^2} + \frac{\varrho\|\mathfrak{E}(t)-\mathfrak{E}_1(t)\|}{\|\mathfrak{R}(t)-\mathfrak{R}_1(t)\|^2} - \frac{\delta}{\|\mathfrak{R}(t)-\mathfrak{R}_1(t)\|}\}\\ \|\mathfrak{R}(t)-\mathfrak{R}_1(t)\|^2. \end{cases} \tag{22}$$

$$< \begin{cases} \gamma_1\|\mathfrak{S}(t)-\mathfrak{S}_1(t)\|^2,\\ \gamma_2\|\mathfrak{E}(t)-\mathfrak{E}_1(t)\|^2,\\ \gamma_3\|\mathfrak{F}(t)-\mathfrak{F}_1(t)\|^2,\\ \gamma_4\|\mathfrak{R}(t)-\mathfrak{R}_1(t)\|^2. \end{cases} \tag{23}$$

Where,

$$\begin{cases} \gamma_1 = & \{\frac{\mu}{\|\mathfrak{S}(t)-\mathfrak{S}_1(t)\|^2} - \frac{\sigma\|\mathfrak{F}(t)-\mathfrak{F}_1(t)\|}{\|\mathfrak{S}(t)-\mathfrak{S}_1(t)\|}\\ & -\frac{\delta}{\|\mathfrak{S}(t)-\mathfrak{S}_1(t)\|}\},\\ \gamma_2 = & \{\frac{\sigma\|\mathfrak{S}(t)-\mathfrak{S}_1(t)\|\|\mathfrak{F}(t)-\mathfrak{F}_1(t)\|}{\|\mathfrak{E}(t)-\mathfrak{E}_1(t)\|^2}\\ & -\frac{(\varrho+\delta+\epsilon)\|\mathfrak{F}(t)-\mathfrak{F}_1(t)\|}{\|\mathfrak{E}(t)-\mathfrak{E}_1(t)\|^2}\},\\ \gamma_3 = & \{\frac{\epsilon\|\mathfrak{E}(t)-\mathfrak{E}_1(t)\|}{\|\mathfrak{F}(t)-\mathfrak{F}_1(t)\|^2} - \frac{(\nu+\delta)}{\|\mathfrak{F}(t)-\mathfrak{F}_1(t)\|}\},\\ \gamma_4 = & \{\frac{\nu\|\mathfrak{F}(t)-\mathfrak{F}_1(t)\|}{\|\mathfrak{R}(t)-\mathfrak{R}_1(t)\|^2} + \frac{\varrho\|\mathfrak{E}(t)-\mathfrak{E}_1(t)\|}{\|\mathfrak{R}(t)-\mathfrak{R}_1(t)\|^2}\\ & -\frac{\delta}{\|\mathfrak{R}(t)-\mathfrak{R}_1(t)\|}\} \end{cases} \tag{24}$$

$(\mathfrak{S},\mathfrak{E},\mathfrak{F},\mathfrak{R})$ is non zero and we have the result

$$< \begin{cases} \gamma_1\|\mathfrak{S}(t)-\mathfrak{S}_1(t)\|\|\mathfrak{S}(t)\|,\\ \gamma_2\|\mathfrak{E}(t)-\mathfrak{E}_1(t)\|\|\mathfrak{E}(t)\|,\\ \gamma_3\|\mathfrak{F}(t)-\mathfrak{F}_1(t)\|\|\mathfrak{F}(t)\|,\\ \gamma_4\|\mathfrak{R}(t)-\mathfrak{R}_1(t)\|\|\mathfrak{R}(t)\|. \end{cases} \tag{25}$$

Based on the findings obtained from Equations (24) and (25), it can be concluded that the employed iterative scheme exhibits stability [9], [10]. □

7 Numerical Simulations

This section aims to showcase a numerical simulation and graphical depiction of the susceptible, infected, exposed and the recovered populations within non-integral SEIR model. This section, we examined the behaviors of susceptible, infected, exposed and the recovered individuals in the fractional-order SEIR model using graphical representations generated by the HWM and ABM methods, as shown in Figure 1, Figure 2, Figure 3, Figure 4, Figure 5, Figure 6, Figure 7, Figure 8, Figure 9, Figure 10, Figure 11, Figure 12, Figure 13, Figure 14.

Figure 1 compares the population of susceptible individuals w.r.t. time using the HWM and ABM methods with parameters $\eta = 4, j = 6$, and $\gamma = 1$. The analysis of Figure 1 reveals that the number of susceptible individuals predicted by both numerical methods is nearly identical, and both methods show a decrease in this number over time. For accurate investigations, we performed evaluations at different fractional order values. Additionally, we analyzed the dynamics of susceptible, infected, exposed, and recovered individuals using Figure 2, Figure 5, Figure 8, Figure 11 for fractional order values of $\gamma = 0.5, 0.6, 0.7, 0.8, 0.9$ in the SEIR model, employing both HWM and ABM methods. Notably, we observed a high infection rate initially, which then slowed over time. Conversely, the recovery rate was initially slow but increased significantly after some time. The comparative analysis of susceptible, infected, exposed and the recovered individuals in the fraction SEIR model is presented graphically for various fractional order values. Figure 4 compares the number of exposed individuals over time for $\eta = 4, j = 6$, and $\gamma = 1$ using both numerical approaches. From this comparison, it can be observed that the behaviours of exposed individuals are similar across both methods in this fractional SEIR model. Additionally, the data reveal that the number of exposed individuals initially increases rapidly with time but then begins to decrease after reaching a certain point in the fractional SEIR model. Additionally, Figure 7 shows that the number of infected individuals decreases over time in the proposed SEIR model . In contrast, Figure 10 illustrates that the number of recovered individuals increases over time for $\eta = 4, j = 6$, and $\gamma = 1$. Figure 3, Figure 6, Figure 9, Figure 12 present a 3D visualization of the SEIR model, illustrating the behaviours of susceptible, infected, exposed, and recovered individuals. In these figures, the three dimensions are represented by the variables γ, time t(in days), and the number of SEIR system individuals. These types of visualizations allow us to observe how the infected, exposed, susceptible, and recovered population changes over time, influenced by the parameter γ, and the factors like transmission rates or other parameters involved in the model. These detailed views help in understanding the dynamic interactions and variations in the infected, susceptible, exposed, and recovered group within the SEIR framework. Figure 13 provides a combined $3D$ representation of the infected, susceptible, exposed, and recovered populations. This visualization allows for a comprehensive view for each group how they evolve over time, illustrating their changes and interactions within the SEIR model.

This visualization allows us to observe how the susceptible, infected, exposed, and recovered population changes over time, influenced by the parameter γ, and the factors like transmission rates or other relevant parameters in the model. This detailed view helps in understanding the dynamic interactions and variations in the susceptible, infected, exposed, and recovered group within the SEIR framework. Figure 13 provides a combined 3D representation of the susceptible, infected, exposed, and recovered populations. This visualization allows for a comprehensive view of how each group evolves over time, illustrating their interactions and changes within the SEIR model.
Table 1, Table 2 and Table 3 highlight the performance of the proposed method compared to the numerical ABM approach. We analyze the populations of susceptible, exposed, infectious, and recovered individuals using $\eta = 4, \gamma = 1$ with varying j values while keeping other parameters consistent with Figure 1 and time t is measured in days. The results show that as j increases, the Hermite wavelet method provides approximations that increasingly align with those from the ABM method. This suggests that the Hermite wavelet method is not only accurate but also increasingly precise as j increases, underscoring its effectiveness and reliability in modeling population dynamics.

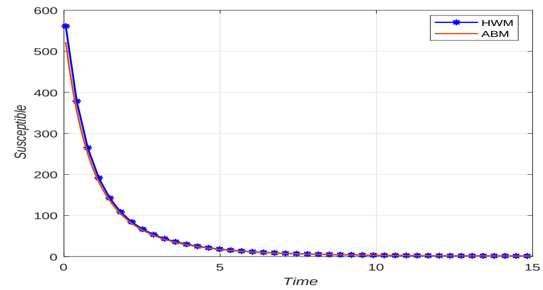

Figure 1: Susceptible individuals plot for the solutions obtained using HWM and ABM at $\eta = 4, j = 6$, and $\gamma = 1$.

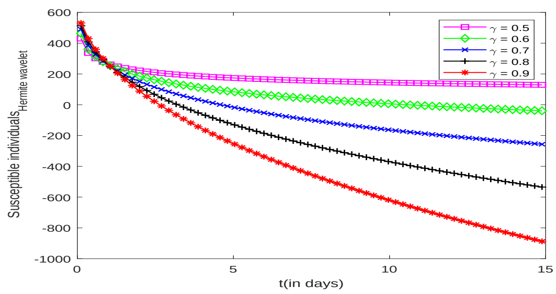

Figure 2: Susceptible individuals plot for different values of γ using HWM with parameters $\eta = 4, j = 5$.

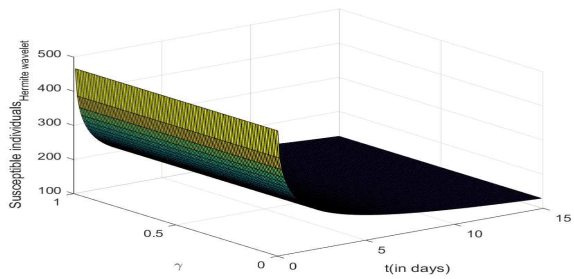

Figure 3: 3D visualization susceptible individuals with parameters $\eta = 4, j = 6$.

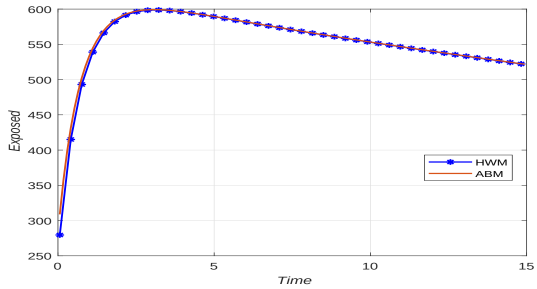

Figure 4: Exposed individuals plot for the solutions obtained using HWM and ABM at $\eta = 4, j = 6$, and $\gamma = 1$.

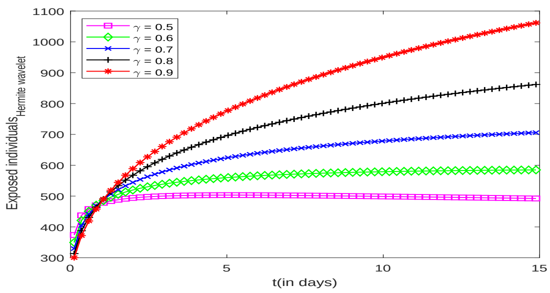

Figure 5: Exposed individuals plot for different values of γ using HWM with parameters $\eta = 4, j = 5$.

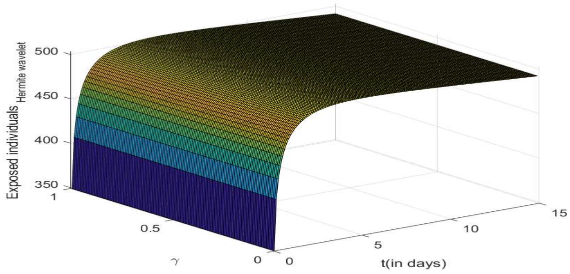

Figure 6: 3D visualization exposed individuals with parameters $\eta = 4, j = 6$.

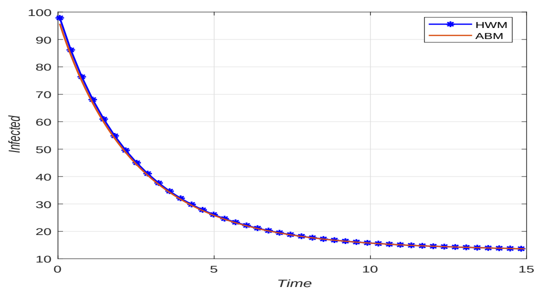

Figure 7: Infected individuals plot for the solutions obtained using HWM and ABM at $\eta = 4, j = 6$, and $\gamma = 1$.

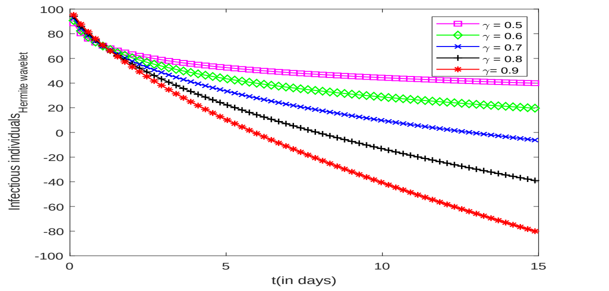

Figure 8: Infected individuals plot for different values of γ using HWM with parameters $\eta = 4, j = 5$.

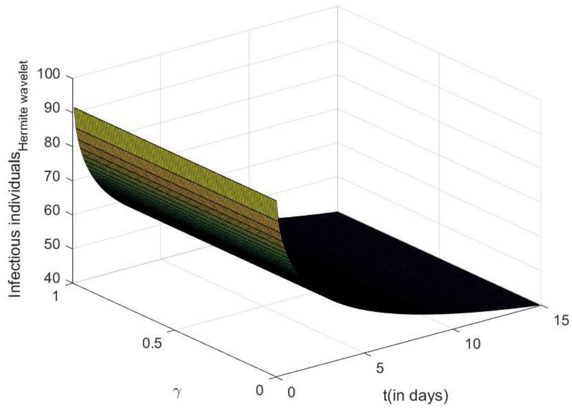

Figure 9: 3D visualization infectious individuals with parameters $\eta = 4, j = 6$.

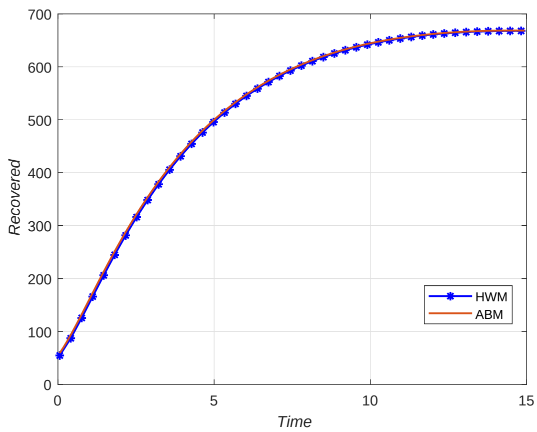

Figure 10: Recovered individuals plot for the solutions obtained using HWM and ABM at $\eta = 4, j = 6$, and $\gamma = 1$.

Nagendra K. Yadav, Rajesh K. Sinha,
Rakesh Ranjan, Ramsingh Yadav

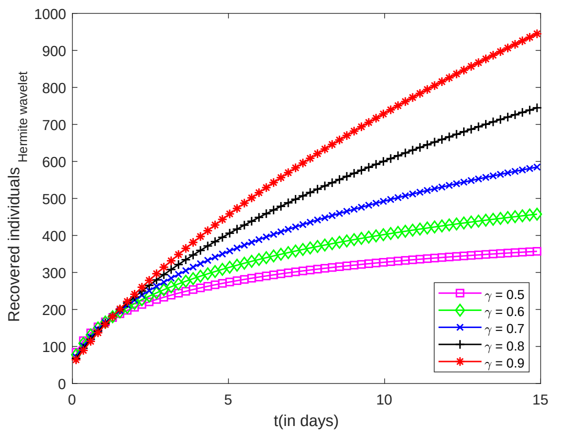

Figure 11: Recovered individuals plot for different values of γ using HWM with parameters $\eta = 4, j = 5$.

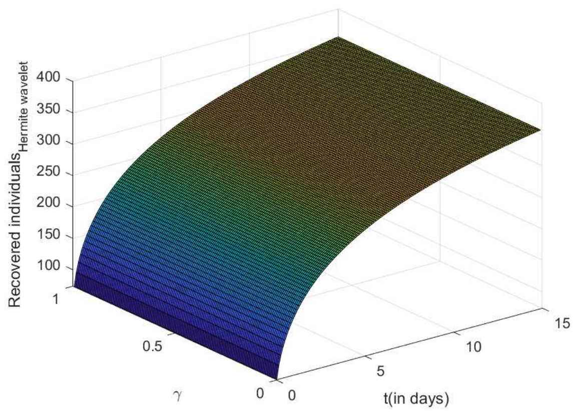

Figure 12: 3D visualization recovered individuals with parameters $\eta = 4, j = 6$.

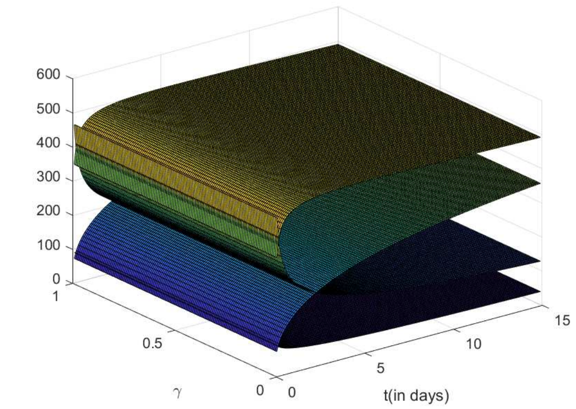

Figure 13: 3D visualization susceptible,exposed,infected and recovered individuals with parameters $\eta = 4, j = 6$.

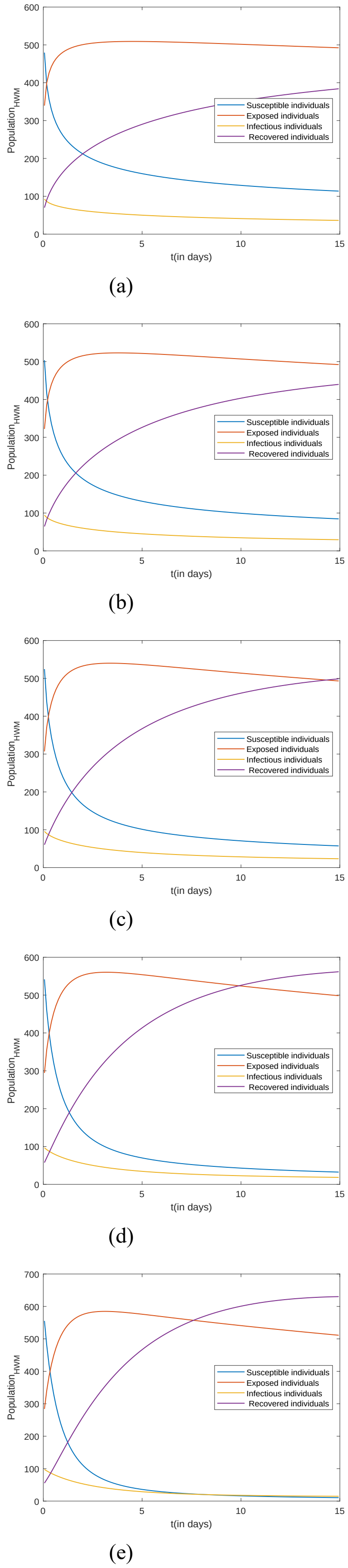

Figure 14: 2D plots of susceptible,exposed, infected and the recovered population across various values of $\gamma = 0.55, 0.65, 0.75, 0.85, 0.95$respectively.

Table 1. Comparison of the findings obtained using proposed technique with those from alternative numerical methods for the populations of susceptible individuals $\mathfrak{S}$, exposed $\mathfrak{E}$, infectious $\mathfrak{F}$, and recovered individuals $\mathfrak{R}$ at $\eta = 4, \gamma = 1$ and $j = 5$.

$Sr.$	t	$\mathfrak{S}_{HWM}$	$\mathfrak{S}_{ABM}$	$\mathfrak{E}_{HWM}$	$\mathfrak{E}_{ABM}$	$\mathfrak{F}_{HWM}$	$\mathfrak{F}_{ABM}$	$\mathfrak{R}_{HWM}$	$\mathfrak{R}_{ABM}$
1	1	213.569	193.388	525.5361	538.0576	70.6831	68.0928	152.6691	167.2428
2	2	94.6254	86.9548	587.8653	591.6891	52.0053	50.3709	263.9912	277.2964
3	3	49.3773	45.1646	598.7683	600.9687	39.7805	38.7304	359.1738	370.432
4	4	28.5707	25.7154	596.0409	598.0015	31.5911	30.9183	435.936	445.4033
5	5	17.7836	15.6405	589.4216	591.4292	26.0526	25.6274	496.4551	504.5013
6	7	8.0321	6.698	574.286	576.4244	19.7018	19.5476	579.7011	585.7961
7	10	3.1955	2.5241	553.0115	555.1598	15.7397	15.7346	643.118	647.6014
8	15	1.4096	1.1704	524.2298	526.2651	13.7513	13.7947	667.836	671.1956

Table 2. Comparison of the result obtained using proposed technique with those from alternative numerical methods for the populations of susceptible individuals $\mathfrak{S}$, exposed $\mathfrak{E}$, infectious $\mathfrak{F}$, and recovered individuals $\mathfrak{R}$ at $\eta = 4, \gamma = 1$ and $j = 6$.

$Sr.$	t	$\mathfrak{S}_{HWM}$	$\mathfrak{S}_{ABM}$	$\mathfrak{E}_{HWM}$	$\mathfrak{E}_{ABM}$	$\mathfrak{F}_{HWM}$	$\mathfrak{F}_{ABM}$	$\mathfrak{R}_{HWM}$	$\mathfrak{R}_{ABM}$
1	1	212.1927	201.5786	526.6416	533.1498	70.6023	69.2815	152.8538	159.8644
2	2	94.9416	91.062	587.6253	589.2821	52.0008	51.1539	264.1833	270.5554
3	3	49.5001	47.6308	598.6368	599.1715	39.7583	39.2045	359.3951	364.7021
4	4	28.6901	27.588	595.9099	596.1844	31.5786	31.2141	436.0765	440.4127
5	5	17.8861	17.1479	589.3065	589.5405	26.0495	25.8096	496.5014	500.0421
6	7	8.0812	7.6815	574.1996	574.467	19.6996	19.5973	579.6971	582.1059
7	10	3.2145	3.0307	552.9433	553.24	15.7392	15.7144	643.0522	644.5011
8	15	1.4138	1.352	524.1699	524.4604	13.7501	13.7524	667.7603	668.5585

Table 3. Comparison of the result obtained using proposed technique with those from alternative numerical methods for the populations of susceptible individuals $\mathfrak{S}$, exposed $\mathfrak{E}$, infectious $\mathfrak{F}$, and recovered individuals $\mathfrak{R}$ at $\eta = 4, \gamma = 1$ and $j = 7$.

$Sr.$	t	$\mathfrak{S}_{HWM}$	$\mathfrak{S}_{ABM}$	$\mathfrak{E}_{HWM}$	$\mathfrak{E}_{ABM}$	$\mathfrak{F}_{HWM}$	$\mathfrak{F}_{ABM}$	$\mathfrak{R}_{HWM}$	$\mathfrak{R}_{ABM}$
1	1	212.1807	206.7153	526.6572	530.0018	70.5968	69.9299	152.906	156.3443
2	2	94.9242	92.9631	587.6307	588.4111	51.9903	51.56	264.257	267.3784
3	3	49.5533	48.6614	598.5921	598.7399	39.7568	39.473	359.431	362.011
4	4	28.7198	28.2362	595.8773	595.8593	31.5755	31.3866	436.1115	438.1896
5	5	17.9119	17.6147	589.2776	589.2225	26.0488	25.9224	496.5127	498.1739
6	7	8.0936	7.9536	574.1781	574.1296	19.6991	19.6421	579.6951	580.7546
7	10	3.2192	3.1621	552.9262	552.8965	15.7391	15.7215	643.0358	643.5795
8	15	1.4149	1.3975	524.1549	524.133	13.7498	13.7465	667.7412	667.9382

8 Conclusion

The primary focus of this paper is the numerical solution of a nonlinear fractional-order SEIR system using the Hermite wavelets collocation method. The SEIR model with fractional derivatives describes systems with memory and hereditary properties, which can be challenging to solve with traditional methods. The proposed nonlinear fractional-order SEIR model has been numerically analyzed through the application of the Adam-Bashforth discretization technique and the Hermite wavelet collocation method.Subsequently, the estimation of function error for the aforementioned waveform, along with an analysis of convergence, has also been examined highlighting its accuracy and effectiveness. By aggregating the collocation points and utilizing an operational matrix (HWOM), it is possible to convert nonlinear FDEs into a system of algebraic equations which are easy to solve. Wavelet method adapt well to the local features of the SEIR fractional model. They can handle non-stationary and transient behaviours more effectively than many classical techniques, providing better insight into the dynamics of disease spread and control. Future work could extend the Hermite wavelet approach applied to fractional order SEIR measles model to other infectious diseases such as influenza, tuberculosis, or COVID-19, incorporating higher-order fractional derivatives, control strategies, and stochastic elements for more robust predictions. Additionally, the Hermite wavelet method combining with other techniques, such as neural networks or machine learning, to create hybrid models that could offer improved predictions and insights into epidemic control strategies.

Declaration of Generative AI and AI-assisted Technologies in the Writing Process

During the preparation of this work the authors used Grammarly for language editing. After using this service, the authors reviewed and edited the content as needed and take full responsibility for the content of the publication.

References:

[1] Ullah, S., Khan, M. A., & Farooq, M. (2018). A new fractional model for the dynamics of the hepatitis B virus using the Caputo-Fabrizio derivative. *European Physical Journal Plus*, 133, 237.

[2] Sols-Pérez, J., Gómez-Aguilar, J., & Atangana, A. (2019). A fractional mathematical model of breast cancer competition model. *Chaos, Solitons & Fractals*, 127, 38-54.

[3] Agarwal, P., & Singh, R. (2020). Modelling of transmission dynamics of Nipah virus (NiV): A fractional order approach. *Physica A: Statistical Mechanics and its Applications*, 547, 124243.

[4] Kilicman, A., et al. (2018). A fractional order SIR epidemic model for dengue transmission. *Chaos, Solitons & Fractals*, 114, 55-62.

[5] Gao, Z., et al. (2013). Models of strategies for control of rubella and congenital rubella syndrome-a 40 year experience from Australia. *Vaccine*, 31, 691-697.

[6] Dubey, V. P., Kumar, R., & Kumar, D. (2020). Numerical solution of time fractional three-species food chain model arising in the

realm of mathematical ecology. *International Journal of Biomathematics*, 13, 2050011.

[7] Baba, I. A., & Ghanbari, B. (2019). Existence and uniqueness of solution of a fractional order tuberculosis model. *European Physical Journal Plus*, 134, 489.

[8] Wu, M., Zhang, J., Huang, Z., Li, X., & Dong, Y. (2023). Numerical solutions of wavelet neural networks for fractional differential equations. *Mathematical Methods in the Applied Sciences*, 46(3), 3031-3044.

[9] Akgul, A. (2019). Reproducing kernel method for fractional derivative with non-local and non-singular kernel. In *Fractional Derivatives with Mittag-Leffler Kernel: Trends and Applications in Science and Engineering* (pp. 1-12).

[10] Akgul, A. (2018). A novel method for a fractional derivative with non-local and non-singular kernel. *Chaos, Solitons & Fractals*, 114, 478-482.

[11] Alshbool, M., Mohammad, M., Isik, O., & Hashim, I. (2022). Fractional Bernstein operational matrices for solving integro-differential equations involving Caputo fractional derivative. *Results in Applied Mathematics*, 14, 100258.

[12] Momoh, A., Ibrahim, M., Uwanta, I., & Manga, S. (2013). Mathematical model for control of measles epidemiology. *International Journal of Pure and Applied Mathematics*, 87(5), 707-717.

[13] Farman, M., Saleem, M. U., Ahmad, A., & Ahmad, M. (2018). Analysis and numerical solution of SEIR epidemic model of measles with non-integer time fractional derivatives by using Laplace-Adomian decomposition method. *Ain Shams Engineering Journal*, 9(4), 3391-3397.

[14] Kermack, W. O., & McKendrick, A. G. (1927). A contribution to the mathematical theory of epidemics. *Proceedings of the Royal Society of London. Series A, Mathematical and Physical Sciences*, 115(772), 700-721.

[15] Kumar, S., Kumar, R., Osman, M. S., & Samet, B. (2021). A wavelet based numerical scheme for fractional order SEIR epidemic of measles by using Genocchi polynomials. *Numerical Methods for Partial Differential Equations*, 37(2), 1250-1268.

[16] Al-Smadi, M. H., & Gumah, G. N. (2014). On the homotopy analysis method for fractional SEIR epidemic model. *Research Journal of Applied Sciences, Engineering and Technology*, 7(18), 3809-3820.

[17] Kumar, S., et al. (2020). An efficient numerical method for fractional SIR epidemic model of infectious disease by using Bernstein wavelets. *Mathematics*, 8, 558.

[18] Yuttanan, B., & Razzaghi, M. (2019). Legendre wavelets approach for numerical solutions of distributed order fractional differential equations. *Applied Mathematical Modelling*, 70, 350-364.

[19] Kumar, S., et al. (2020). A study of fractional Lotka-Volterra population model using Haar wavelet and Adams-Bashforth-Moulton methods. *Mathematical Methods in the Applied Sciences*, 43, 5564-5578.

[20] Yadav, P., Jahan, S., & Nisar, K. S. (2024). Fibonacci wavelet method for time fractional convection-diffusion equations. *Mathematical Methods in the Applied Sciences*, 47(4), 2639-2655.

[21] Panda, S. K., Abdeljawad, T., & Ravichandran, C. (2020). A complex valued approach to the solutions of Riemann-Liouville integral, Atangana-Baleanu integral operator and non-linear telegraph equation via fixed point method. *Chaos, Solitons & Fractals*, 130, 109439.

[22] Ravichandran, C., et al. (2020). On new approach of fractional derivative by Mittag-Leffler kernel to neutral integro-differential systems with impulsive conditions. *Chaos, Solitons & Fractals*, 139, 110012.

[23] Kumbinarasaiah, S., & Adel, W. (2021). Hermite wavelet method for solving nonlinear Rosenau–Hyman equation. *Partial Differential Equations and Applied Mathematics*, 4, 100062.

[24] Ebadian, A., & Khajehnasiri, A. A. (2014). Block-pulse functions and their applications to solving systems of higher-order nonlinear Volterra integro-differential equations. *Electronic Journal of Differential Equations*, 2014(54), 1-19.

Contribution of Individual Authors to the Creation of a Scientific Article (Ghostwriting Policy)

The authors equally contributed in the present research, at all stages from the formulation of the problem to the final findings and solution.

Sources of Funding for Research Presented in a Scientific Article or Scientific Article Itself

No funding was received for conducting this study.

Conflict of Interest

The authors have no conflicts of interest to declare.